

Biodegradable Nanoagents with Short Biological Half-Life for SPECT/PAI/MRI Multimodality Imaging and PTT Therapy of Tumors

Lei Chen, Jiayao Chen, Shanshan Qiu, Ling Wen, Yan Wu, Yi Hou, Yong Wang, Jianfeng Zeng,* Yuan Feng, Zhen Li, Hong Shan,* and Mingyuan Gao*

Rapid clearance of nanoagents is a critical criterion for their clinical translation. Herein, it is reported that biodegradable and renal clearable nanoparticles are potentially useful for image-guided photothermal therapy of tumors. The multifunctional nanoparticles with excellent colloidal stability are synthesized through coordination reactions between Fe^{3+} ions and gallic acid (GA)/polyvinyl pyrrolidone (PVP) in aqueous solution. Detailed characterization reveals that the resulting Fe^{3+} /GA/PVP complex nanoparticles (FGPNs) integrate strong near-infrared absorption with paramagnetism well. As a result, the FGPNs present outstanding performance for photoacoustic imaging and magnetic resonance imaging of tumors, and outstanding photothermal ablation effect for tumor therapy owing to their high photothermal conversion efficiency. More importantly, the pharmacokinetic behaviors of the FGPNs determined through ^{125}I labeling suggest that the FGPNs are readily degraded in vivo showing a short biological half-life, and the decomposition products are excreted through either renal clearance pathway or bowel elimination pathway via stomach, which highlights the characteristics of the current multifunctional theranostic agent and their potential in clinical translation.

have been developed based on different diagnostic and therapeutic combinations to satisfy specific and individualized theranostic strategies, such as magnetic resonance imaging (MRI)/photothermal therapy (PTT),^[6,7] photoacoustic imaging (PAI)/PTT,^[8,9] positron emission tomography (PET)/PTT,^[10] computed tomography (CT)/PAI/PTT,^[11,12] optical imaging (OI)/photodynamic therapy (PDT)/PTT,^[13] MRI/PAI/PTT,^[14] single-photon emission computed tomography (SPECT)/MRI/OI,^[15] and OI/MRI-PAI-PDT/PTT,^[16] while the combination of different imaging modalities, often called multimodality imaging, can overcome the limitations of each imaging modality and thus more precisely pinpoint the cancerous areas for imaging-guided tumor therapy.

Compared to the small molecular intravenous drugs, nanotheranostic agents possess distinct advantages due to their longer blood residence time, engineerable functions, and strongly enhanced uptake and retention within tumors.^[3,4,17–21] However, different from the small molecular agents that are largely excreted through the urinary system within a short period, systematically delivered nanoparticles are usually cleared from the blood stream and then delivered to reticuloendothelial system

1. Introduction

Nanotheranostic agents integrated with diagnostic and therapeutic functions hold great promise in cancer imaging and therapy.^[1–5] To date, a large number of nanotheranostic agents

L. Chen, S. S. Qiu, Dr. L. Wen, Dr. Y. Wu, Prof. Y. Wang, Dr. J. F. Zeng, Prof. Y. Feng, Prof. Z. Li, Prof. M. Y. Gao
Center for Molecular Imaging and Nuclear Medicine
School for Radiological and Interdisciplinary Sciences (RAD-X)
Soochow University
Suzhou 215123, China
E-mail: jfzeng@suda.edu.cn; gaomy@iccas.ac.cn

L. Chen, S. S. Qiu, Dr. L. Wen, Dr. Y. Wu, Prof. Y. Wang, Dr. J. F. Zeng, Prof. Y. Feng, Prof. Z. Li, Prof. M. Y. Gao
Collaborative Innovation Center of Radiation Medicine
of Jiangsu Higher Education Institutions
Suzhou 215123, China

J. Y. Chen, Prof. H. Shan
Department of Interventional Medicine
The Fifth Affiliated Hospital
Sun Yat-sen University
Zhuhai 519000, China
E-mail: shanhong@mail.sysu.edu.cn

Prof. H. Shan
Guangdong Provincial Engineering Research Center
of Molecular Imaging
The Fifth Affiliated Hospital
Sun Yat-sen University
Zhuhai 519000, P. R. China
Prof. Y. Hou, Prof. M. Y. Gao
Institute of Chemistry
Chinese Academy of Sciences
Beijing 100190, China
Prof. M. Y. Gao
School of Chemistry and Chemical Engineering
University of Chinese Academy of Sciences
Beijing 100049, P. R. China

DOI: 10.1002/sml.201702700

(RES) including liver and spleen.^[22,23] Although appropriate surface modification, e.g., polyethylene glycol (PEG), zwitterion, peptide, and protein coating, can suppress the RES uptake,^[19,21,24–27] the majority of nanoparticles remain accumulated in RES organs, resulting in potential toxicity risk. Therefore, it is necessary to develop nanoparticles with short biological half-life. One way to shorten the biological half-life is to reduce the particle size as many ultrasmall nanoparticles are found to be renal clearable, such as ultrasmall quantum dots,^[28] C dots,^[29] rare-earth nanoparticles,^[30] metal oxides/sulfides/selenides nanoparticles,^[31–33] and gold nanoparticles.^[34] The other way is to use biodegradable materials to construct the theranostic particles.^[35] Studies have shown that many kinds of inorganic nanoparticles are biodegradable in vivo, such as iron oxide nanoparticles^[23,36] and silica nanoparticles^[37] that exhibit broad biomedical applications. However, their degradation kinetics is typically slow and strongly dependent on chemical nature of the materials forming the nanoparticle cores, apart from impacts of the particle size and surface property. Although the biodegradability of polymer particles can largely be tuned through proper design of the macromolecular structure, typically as drug carriers, it takes long time for them to be degraded under physiological conditions.^[38] In contrast, particles formed upon self-assembly of small molecular complexes may offer an alternative

way due to the weak intermolecular interactions. For example, we recently have demonstrated the self-assembled Fe(III)–gallic acid (GA) nanoparticles are stable in tumors, but are rapidly dissociated in normal organs/tissues because of the pH-dependent aggregating behavior of the Fe(III)–GA complex.^[39]

Although the self-assembled nanoparticles formed by Fe³⁺ ion and gallic acid present excellent performance for PTT and PAI of tumors, they are very instable in acidic range. Herein, we make use of the pH dependent agglomeration of Fe³⁺/GA complexes, but in difference, introduce polyvinyl pyrrolidone (PVP) as a particle surface capping agent. Taking the advantage of multidentate coordination capacity of PVP for Fe(III),^[40] colloiddally stable Fe³⁺/GA/PVP nanoparticles (FGPNs) with ultrasmall size were designed. By further labeling the resulting particles with ¹²⁵I, the pharmacokinetic behaviors and in particular the metabolism of the resulting particles were investigated.

2. Results and Discussion

2.1. Synthesis and Characterization of FGPNs

The synthesis of FGPNs is schematically shown in Figure 1a. It is known that Fe³⁺/GA complexes can be formed upon the

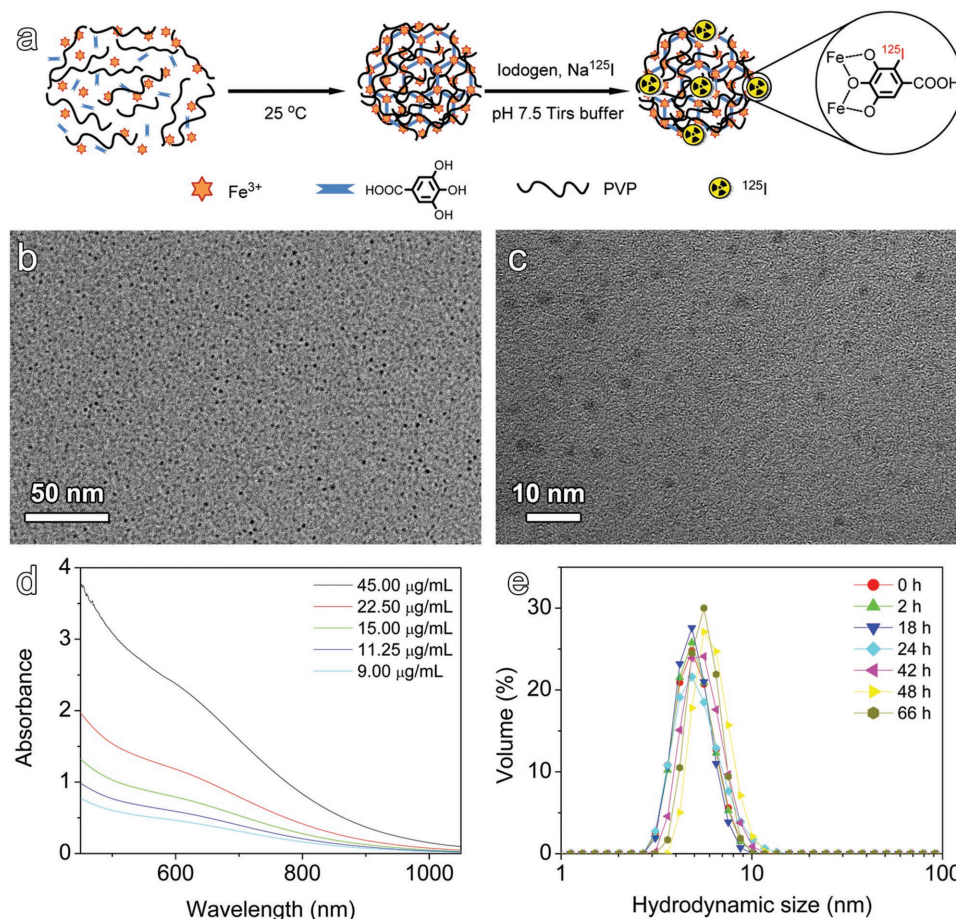


Figure 1. Synthesis and characterization of FGPNs. a) Schematic illustration of the synthesis and radiolabeling of FGPNs. b) TEM image of the as-prepared FGPNs. c) HRTEM image of the as-prepared FGPNs. d) UV-vis-NIR absorbance spectra of FGPNs solution with different iron concentrations. e) Hydrodynamic size distribution profiles of FGPNs after incubated in pure water for different periods of time.

coordination interaction between Fe^{3+} and gallic acid through its catechol group. The protonation of carboxylate groups of gallic acid can further induce the self-assembly of complexes into small nanoparticles at lowered pH.^[39] However, the agglomeration of the molecular complexes is rather uncontrollable giving rise to much bigger particles and even precipitation against time. To effectively regulate the particle growth, PVP was introduced into the system. In brief, by mixing FeCl_3 , PVP, and gallic acid in aqueous solutions under the ambient conditions, the FGPNs were obtained.

Due to the remarkable stabilization effect of PVP, the FGPNs obtained are rather uniform and characterized by ultrasmall average size of 2.0 ± 0.2 nm according to transmission electron microscopy (TEM) and high-resolution TEM (HRTEM) results given in Figure 1b,c, respectively. The corresponding size distribution profile is shown in Figure S1 (Supporting Information). The X-ray diffraction pattern in Figure S2 (Supporting Information) indicated that the resulting nanoparticles are amorphous. Owing to the $d-d$ transition, they present a strong absorption below 900 nm (Figure 1d), which makes them desirable for PAI and PTT. Extensive analysis combining X-ray photoelectron spectroscopy, elemental analysis, and thermogravimetric analysis revealed that the mass fraction of iron, gallic acid, and PVP in the as-prepared FGPNs is 4.08%, 15.72%, and 72.78%, respectively (Figures S3 and S4 and Table S1, Supporting Information). Due to the sufficiently high PVP content, the FGPNs obtained present excellent colloidal stability in pure water, phosphate buffered saline (PBS) as well as 2-[4-(2-hydroxyethyl)-1-piperazinyl] ethanesulfonic acid (HEPES) media, as shown in Figure 1e and Figure S5 (Supporting Information). The hydrodynamic size and zeta potential in pure water is 6.0 nm and -8.5 mV, respectively.

2.2. Relevant Properties of FGPNs for PTT, PAI, and MRI

The ultrasmall size and strong near-infrared (NIR) absorption, together with the excellent colloidal stability under physiological conditions make the FGPNs very suitable for PAI and PTT of tumors. To determine their photothermal conversion efficiency, a series of solutions containing different concentrations of FGPNs were prepared and exposed to an 808 nm continuous-wave (CW) laser irradiation with a power density of 0.5 W cm^{-2} . The photothermal images (Figure 2a) and temperature variation (Figure 2b) of each solution were carefully recorded during the illumination process. It is evident that the temperature increment (ΔT) of the FGPNs solutions positively increases against the particle concentration. The maximum ΔT is around 28.3°C for the solution containing the highest concentration of FGPNs in the tested concentration range, i.e., $45 \mu\text{g mL}^{-1}$, in huge contrast to that (2.3°C) for pure water with identical volume. To further show the photothermal stability, the temperature variation of FGPNs solution with a concentration of $22.5 \mu\text{g mL}^{-1}$ was monitored for five successive cycles of laser irradiation followed by natural cooling process. As shown in Figure 2c, the temperature curve recorded during the first heating/cooling cycle is well-reproduced through the following cycles, indicating that the FGPNs possess excellent photothermal stability under the laser irradiation, which is also supported by the fact that the absorption spectrum and

hydrodynamic size of the FGPNs did not show obvious change after five heating/cooling cycles (Figure S6, Supporting Information). Based on the above results, the photothermal conversion efficiency of the FGPNs was calculated to be $67.4 \pm 5.1\%$ (Figure S7 and Table S2, Supporting Information), comparable to that of Fe^{3+} /GA complexes particles formed in the absence of PVP.^[39] The high photothermal conversion efficiency can probably be attributed to the high absorption/scattering ratios and effective nonradiative electron relaxation dynamics. All the above results suggest that FGPNs would be a suitable photothermal agent for cancer therapy.

In addition, the excellent photothermal conversion performance shown above also enables the FGPNs as contrast agent for PAI.^[41–43] To further characterize the PAI capacity, the photoacoustic images of a series of FGPNs solutions were acquired under excitation of 680, 720, 760, 808, and 850 nm, respectively (Figure 2d). The photoacoustic signals against particle concentrations were then plotted in Figure 2e. The excellent linearity independent of the excitation wavelength offers the possibility for quantifying the imaging results. The amplification factor of the photoacoustic signal, i.e., the slope of regression line in Figure 2e, decreases strongly against the excitation wavelength, but well in accordance with the extinction coefficient of the FGPNs, as shown in Figure S8 (Supporting Information). This is because the PAI is obtained through photothermal conversion of the FGPNs; higher extinction coefficient is therefore favorable for stronger photoacoustic signal. Nevertheless, the above results demonstrate that FGPNs can be used in a broad spectroscopic range as imaging agents for PAI, which is favorable for quantified imaging studies.

Apart from the outstanding photothermal conversion performance for PTT and PAI, the ferric ions incorporated make the FGPNs potentially useful as contrast agent for MRI. To evaluate the magnetic resonance enhancement effect of the FGPNs, relaxivity measurements were performed on a 3 T MRI scanner at room temperature. The longitudinal (r_1) and transverse (r_2) relaxivity of the FGPNs were determined to be 2.16 and $3.09 \text{ mM}^{-1} \text{ s}^{-1}$ (Figure 2f), respectively. The r_2/r_1 of 1.43 suggests that FGPNs can be used as an efficient T_1 contrast agent,^[44] although the longitudinal relaxivity is slightly lower than that of clinic gadolinium-based contrast agents of $3.15 \text{ mM}^{-1} \text{ s}^{-1}$,^[45] it was comparable to that of ferric complex-based MRI contrast agents.^[46] The T_1 -weighted MRI results on FGPNs solutions with different concentrations as shown in Figure S9 (Supporting Information) revealed that substantial enhancement effect could be observed even when the iron concentration was down to $0.2 \times 10^{-3} \text{ M}$.

2.3. Cytotoxicity of FGPNs

The cytotoxicity of FGPNs was evaluated through standard methyl thiazolyl tetrazolium assays on the proliferation of 4T1 cells (murine breast cancer cells) and 3T3 cells (mouse fibroblast cells). The results given in Figure S10 (Supporting Information) revealed that FGPNs exhibited nearly no toxicity to both tumor cells and normal cells when the iron concentration was below 10 mg L^{-1} . The cell viability remained above 60% even when the iron concentration was increased to

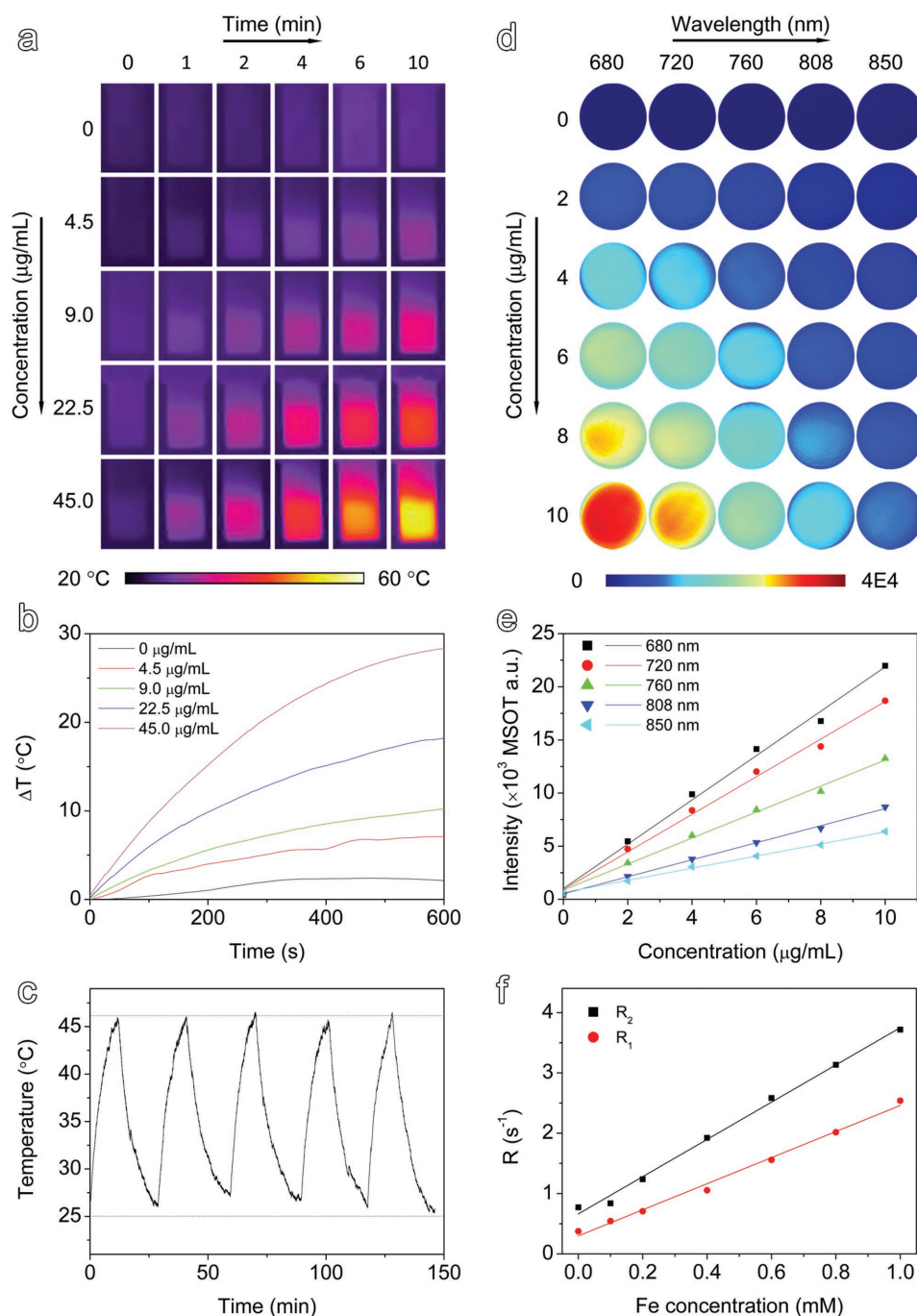


Figure 2. PTT, PAI, and MRI of solutions containing different concentrations of FGPNs. a) Thermal images of FGPNs solutions under 808 nm laser irradiation with a power density of 0.5 W cm^{-2} . b) Temperature variation curves of FGPNs solutions with different iron concentrations as a function of irradiation time. c) Temperature variation curves of FGPNs solution ($22.5 \mu\text{g Fe mL}^{-1}$) recorded during five continuous heating/cooling cycles. d) Photoacoustic images of FGPNs solutions with different iron concentrations captured under excitation at different wavelengths. e) Photoacoustic signal intensity of particle solutions as a function of iron concentration. f) R_1 and R_2 relaxivities of FGPNs as a function of iron concentration.

20 mg L^{-1} (corresponding to a concentration of 490 mg L^{-1} FGPNs). The biocompatibility of FGPNs is expected because all the components of FGPNs, including ferric ions, gallic acid, and PVP, are biocompatible and have a low cytotoxicity.^[47–49] The above results further indicate that a dose of $5 \text{ mg Fe per kg body weight}$ is appropriate for in vivo studies to avoid the toxicity effect.

2.4. In Vivo PAI and MRI with FGPNs

The PAI of tumors in vivo was performed on mice with 4T1 tumors after intravenous injection of $200 \mu\text{L}$ of FGPNs (containing $50 \mu\text{g Fe}$) through the tail vein. The photoacoustic signals of the tumor site were acquired before and at different

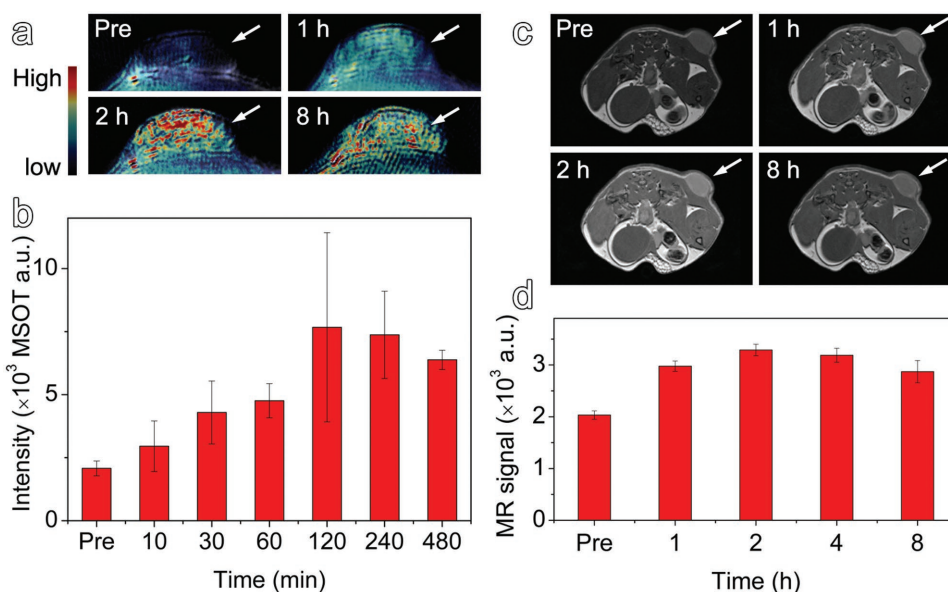


Figure 3. In vivo PAI and MRI of tumor xenografts. a) Photoacoustic images of tumor site before injection and at different time points postinjection with FGPNs. b) Photoacoustic signal of the tumor site as a function of postinjection time. c) Magnetic resonance images of the tumor site before injection and at different time points postinjection with FGPNs. d) Relative magnetic resonance signal of the tumor site as a function of postinjection time.

time points postinjection, under excitation at 680, 720, 760, 808, and 850 nm, respectively. **Figure 3a** shows the photoacoustic images of the tumorous site obtained through imaging construction and spectrum unmixing. The overall contrast of the tumor site is gradually increased after the injection of the FGPNs and reaches a maximum at 2 h postinjection. The quantified results given in **Figure 3b** reveal that the photoacoustic signal is enhanced by a factor of 3.7 compared to the precontrast one, indicating the FGPNs can effectively be uptaken through the enhanced permeation and retention effect of tumors.

To disclose the capacity of the FGPNs as contrast agent for MRI of tumors, BALB/c mice bearing 4T1 tumors were intravenously injected with the same dose of FGPNs used for PAI. The T_1 -weighted images acquired on a 3 T small animal MRI scanner, as shown in **Figure 3c**, reveal that the contrast of the tumor site is gradually increased against time and reaches a maximum at 2 h postinjection, rather consistent with trend for PAI. But the maximum MRI signal of the tumor is increased by 62% (**Figure 3d**) in comparison with that recorded precontrasted, indicating that FGPNs are not only suitable for PAI but also for MRI of tumors.

2.5. Pharmacokinetic Behaviors of FGPNs

Pharmacokinetics is one of the core issues closely related to in vivo applications of nanoparticles. It is not only about the tumor uptake of nanoparticles, but also the undesirable biodistribution leading to potential side effects. To sensitively detect the biodistribution and elimination pathways, the FGPNs were labeled with ^{125}I through phenolic group of gallic acid through the commonly used iodogen method, a radiolabeling yield of higher than 60% was obtained after 30 min reaction. The radiochemical purity was $\approx 98.5\%$ through two cycles of ultrafiltration using 30 kDa molecular weight cut-off (MWCO) centrifugal filter (**Figure S11**,

Supporting Information). Owing to the low quantity of radionuclide, ^{125}I labeling did not lead to an evident change of the hydrodynamic size of the FGPNs, as shown in **Figure S12** (Supporting Information), which is important for accurately tracing the nanoparticles in vivo through gamma signal of ^{125}I . In addition, ^{125}I labeling also provides a possibility to image tumors with SPECT.

After intravenous injection of ^{125}I -labeled FGPNs (200 μL containing 50 μg Fe and 150 μCi ^{125}I , corresponding to 2.5 mg Fe and 7.5 mCi ^{125}I per kg body weight), the mice bearing 4T1 tumors were imaged using a small animal SPECT/CT scanner. The representation images acquired at different time points postinjection are shown in **Figure 4a**. The imaging results suggest that the FGPNs were mainly localized in the bloodstream at the initial stage, as evidenced by the strong signal from the heart as well as major blood vessels and vascular organs. Then, they are gradually eliminated from blood and accumulated in tumor and other organs including bladder, stomach, liver, intestine, and thyroid. After approximately 48 h, the radioactive signals from all above organs nearly vanish except for the thyroid.

To further quantify the SPECT results, the volume of interest of desired organs or tissues were selected for calculating the biodistributions of the FGPNs, expressed by percentage of the injected dose (% ID) or percentage of the injected dose per gram (% ID g^{-1}) (**Figure 4b–j**). It can be found that the maximum tumor uptake (5.3% ID g^{-1}) appears at 2.5 h postinjection. This is generally in good agreement with the PAI and MRI results shown in **Figure 4b**. The results given in **Figure 4c** reveal that the radioactive signal from blood remains detectable 8 h postinjection, suggesting that the FGPNs possess a long blood residence time. Further fitting the signal profile of blood with a two-compartment model resulted in a distribution half-life ($t_{1/2,\alpha}$) of 53 min and an elimination half-life ($t_{1/2,\beta}$) of 383 min (**Figure S13**, Supporting Information). The relatively long blood half-life explains the effective accumulation of the FGPNs in tumors. In addition, the

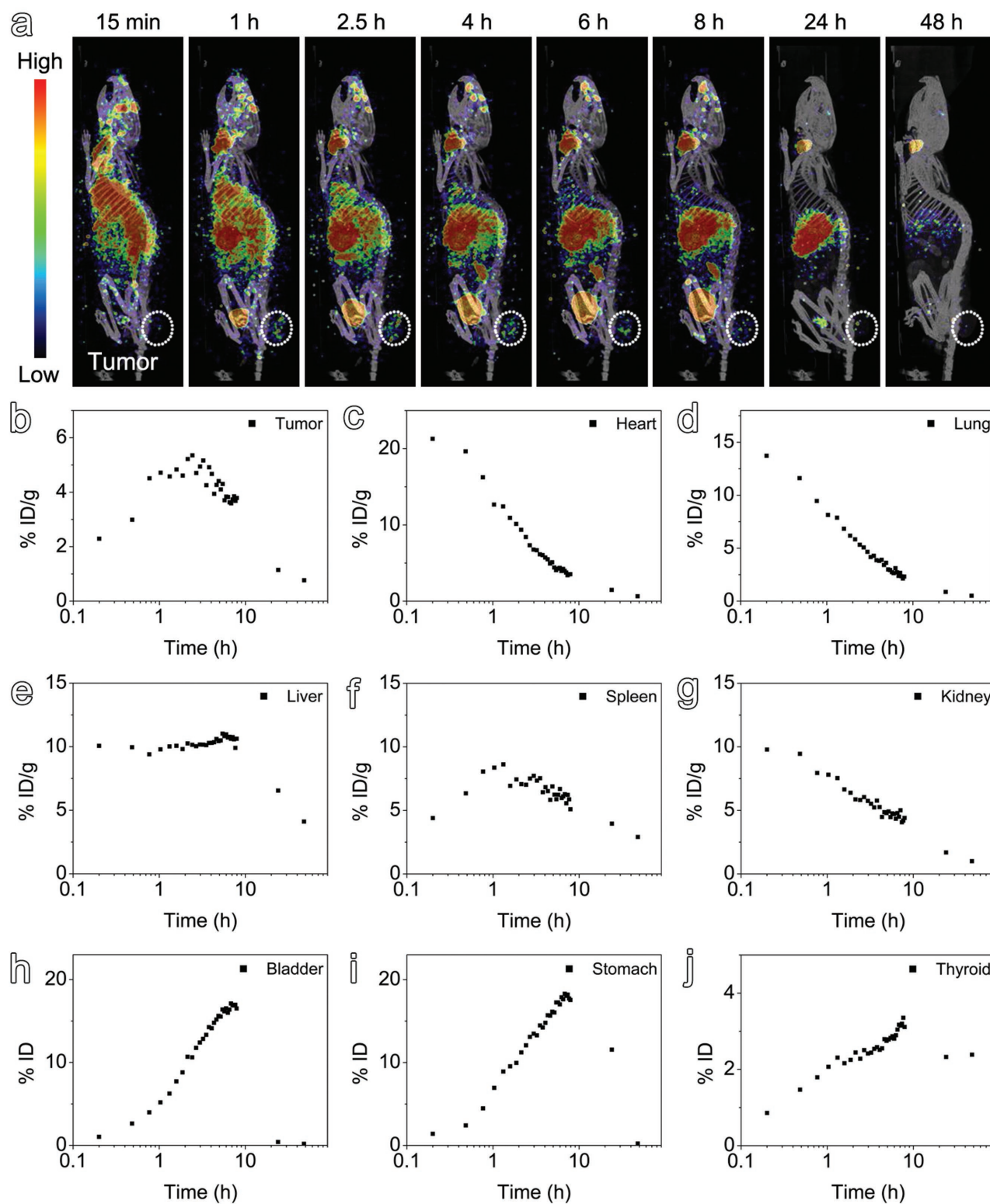


Figure 4. SPECT-CT images and biodistribution of FGPNs in tumor tissue and different organs. a) 3D SPECT-CT images of a mouse bearing tumor xenograft acquired at different time points postinjection of ^{125}I -labeled FGPNs. b–j) Temporal distribution of FGPNs in tumor and different organs, e.g., tumor, heart, lung, liver, spleen, kidney, bladder, stomach, and thyroid, acquired after injection of ^{125}I -labeled FGPNs.

lung presents a very similar signal profile to blood (Figure 4d), indicating that the radioactivity in lung mainly comes from the blood and the lung uptakes nearly no FGPNs. In difference, as shown in Figure 4e, the liver distribution of the FGPNs presents a plateau at approximate 10% ID g⁻¹ in the initial stage and then gradually decreases from 6 h postinjection. Given the higher nanoparticle concentration in blood at the earlier stage, the liver actually has a slow uptake of nanoparticles in the initial time, giving rise to a particle distribution profile similar to spleen as shown in Figure 4f, although the maximum uptake of liver appears later than that of spleen. Nevertheless, the distributions of FGPNs in liver and spleen are much lower than many other kinds of nanoparticles as previously reported,^[50–54] indicating the FGPNs can effectively evade the immune uptake probably due to their ultrasmall hydrodynamic size and excellent biocompatibility. In addition, the ultrasmall hydrodynamic size generally favors the renal clearance of the FGPNs through kidney, which is supported by the slowly decreased kidney signal (Figure 4g) and gradually increased bladder signal (Figure 4h). The above quantified results also reveal that approximate 16.5% of the injected nanoparticles are excreted through renal clearance pathway at 8 h postinjection.

Similar to bladder, the stomach also presents a gradually increased signal (Figure 4i), which was not found in the previous pharmacokinetics studies on nanoparticles.^[28,53–55] In general, nanoparticles intravenously delivered are hardly eliminated through bowel pathway via stomach. It can thus be deduced that the stomach signal may come from detached radioiodinated fragment of the FGPNs. It was reported that weak acid or basic small molecular drugs can irreversibly pass the lipid membrane on stomach and then are secreted into gastric juice.^[56] As gallic acid possesses carboxyl and phenolic groups, it may enter the stomach together with firmly bound ¹²⁵I. To verify this hypothesis, ¹²⁵I-labeled gallic acid (¹²⁵I-GA) was adopted as a control. The SPECT/CT imaging together with the quantified temporal stomach signal shown in Figure S14 (Supporting Information) revealed that the stomach signal quickly increased against time and reached a plateau 2 h postinjection, suggesting that the stomach signal comes from ¹²⁵I-GA formed in consequence of the degradation of FGPNs in vivo. Thus, the degradation of the FGPNs under physiological conditions was further investigated by monitoring the variation of the radiochemical purity of ¹²⁵I-label FGPNs in saline. The results shown in Figure S15 (Supporting Information) revealed that the radiochemical purity of ¹²⁵I-labeled FGPNs was gradually decreased to 90% after 4 h and further down to 60% after 72 h in saline. The instability acquired through the radioactivity signal detection may arise from the release of ¹²⁵I-GA due to the degradation of the FGPNs or deiodination (radioiodine dissociates from the ortho-position of phenolic group) as commonly observed. However, the radioactive distribution profile in thyroid (Figure 4j) suggests that the decreased instability is dominated by the release of ¹²⁵I-GA as the maximum thyroid uptake is only of 3.3% ID. In addition, the degradable property of FGPNs was also strongly evidenced by the in vitro dialysis experiments, which showed a sustained release of ferric ions from FGPNs (Figure S16, Supporting Information). A total of 3.4% of the iron in FGPNs was found in dialysate after being dialyzed against pure water for 3 d.

As required by food and drug administration that all the injected imaging agents must be cleared in a reasonable period of

time,^[28] the long retention in vivo has become a major hurdle for clinical translation of most nanoparticles developed for imaging applications. The above results demonstrate that the FGPNs as a novel alternative of inorganic nanoparticles are biodegradable after intravenous injection, thus showing a short biological half-time of 20.5 h according to the results given in Table S3 (Supporting Information) and Figure S17 (Supporting Information). Nevertheless, the biological half-life is long enough for tumor imaging and therapy, as only 2–3 h is required for the FGPNs to reach the maximum tumor uptake. All these excellent features make the FGPNs superior to the common inorganic nanoparticles-based theranostic agents. In addition, the degradation products including ferric ions, PVP, and gallic acid, are low toxic, which is another unique characteristic of the current FGPNs.

2.6. Photothermal Ablation of Tumors with FGPNs

Encouraged by the high photothermal conversion efficiency and the tumor targeting ability aforementioned, in vivo PTT experiments were carried out. In detail, BALB/c mice bearing 4T1 tumors were randomly divided into four groups (*n* = 5). The mice of the treatment group were intravenously injected with FGPNs (200 μ L containing 50 μ g Fe) and then irradiated for 10 min by 808 nm laser with a power density of 1 W cm⁻² 2.5 h postinjection. The rest groups were used as controls. The first group of mice received only saline injection, the second group of mice was subjected to laser irradiation after saline injection, and the third group was injected with FGPNs without laser irradiation being applied. During the PTT studies, the photothermal images were also recorded with an infrared imaging camera to monitor the temperature variation of the tumor sites. As shown in Figure 5a, the tumor local temperature of the mice receiving the FGPNs increases more dramatically than that of mice receiving saline injection. As shown in Figure 5b, 10 min laser irradiation can dramatically increase the tumor local temperature to 51.6 °C, which is more than sufficient to ablate the tumors.

The representative photographs of mice and the temporal tumor size are shown in Figure 5c,d, respectively. It clearly shows that the tumors of the treatment group shrank remarkably after photothermal treatment and completely eradicated 21 d after PTT treatment. In addition, no obvious body weight variation was observed in the four groups of mice after various treatments (Figure 5e), indicating that the FGPNs have no significant harmful side effect for in vivo applications and thus can potentially be used as an effective PTT agent for cancer treatment.

2.7. Biosafety of FGPNs

To further assess the potential toxicity of the FGPNs, healthy BALB/c mice were intravenously injected with a dose of the FGPNs identical to those used for both PAI/MRI and PTT treatment. The mice were sacrificed at 1, 8, and 30 d postinjection for routine blood examination through blood chemistry and histological analysis (*n* = 5). Another group of five healthy mice receiving no particle injection was set as control. The blood analysis results shown in Figure 6a,b reveal that no significant difference for all parameters associated with acute toxicity can

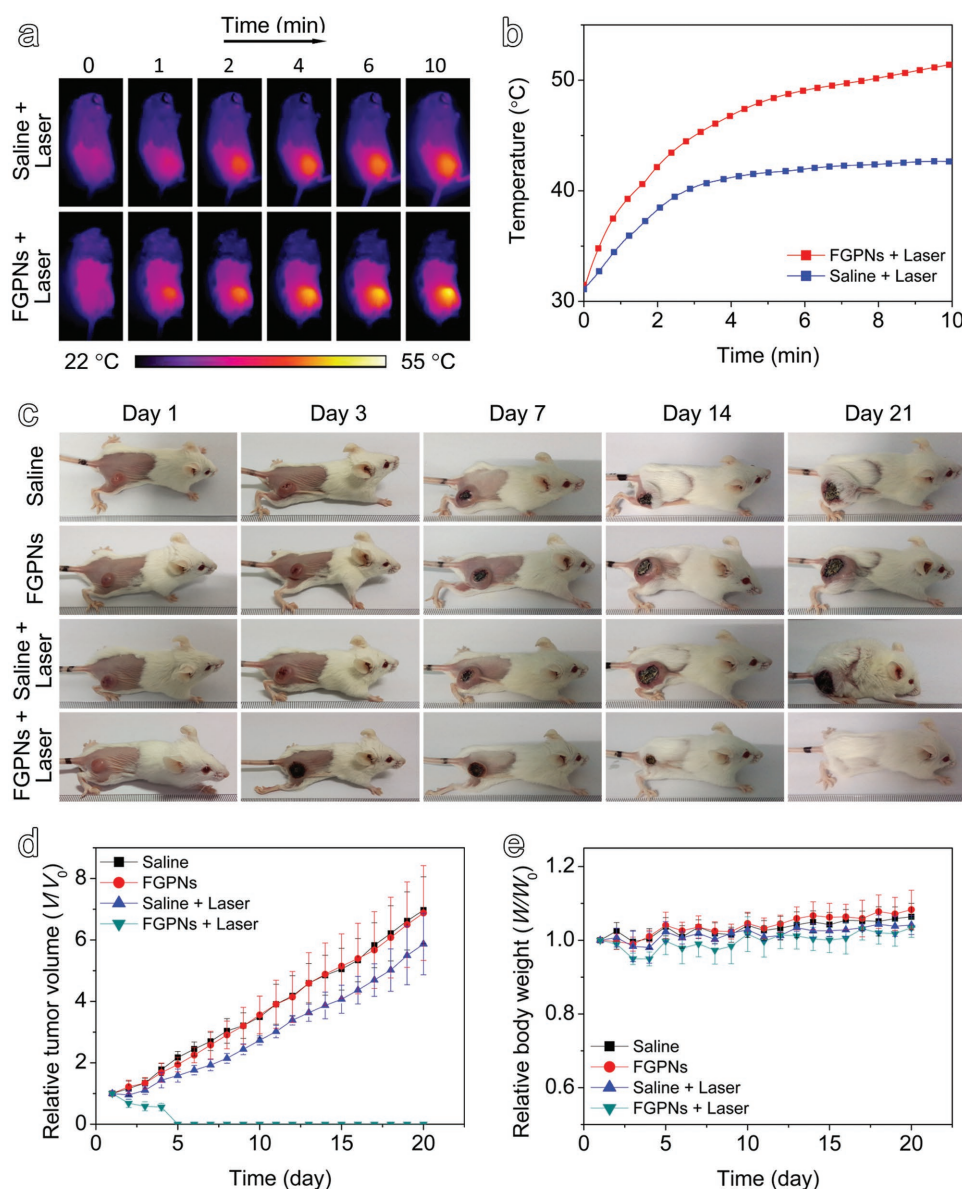


Figure 5. Photothermal therapy of tumors in vivo using FGPNs. a) Thermal images of tumor-bearing mice injected with saline (upper row) or FGPNs (lower row) (irradiation source: 808 nm laser, 1.0 W cm^{-2} , 10 min). b) Tumor local temperature recorded during laser irradiation. c) Representative photographs of tumor-bearing mice receiving different treatments indicated. d) The tumor growth curves for different groups of mice recorded after different treatments. e) Body weight curves of mice in different groups recorded after different treatments.

be observed if comparing the treatment groups with the control group. The histological analysis (Figure 6c) further reveals that no noticeable inflammation or damage in any of the major organs was induced by the intravenously injected FGPNs. All above results suggest that FGPNs are rather safe at the current dose level for theranostic applications.

3. Conclusion

In summary, ultras-small FGPNs have been synthesized by using PVP as a surface capping agent for stabilizing the nanoparticles formed by ferric ion and gallic acid. The excellent colloidal stability together with the intrinsic photothermal

conversion ability and paramagnetism of Fe/GA complexes enable the resulting FGPNs useful for PAI/MRI and PTT of tumors. Most importantly, the systematic pharmacokinetic studies based on ^{125}I labeling reveal that the FGPNs possess excellent biodegradable properties and thus present a short biological half-life which however well meets the requirement for the following tumor theranostic applications. In addition, the renal clearance pathway and bowel elimination pathway via stomach are mainly taken by the FGPNs and the degradation products. The blood chemistry and tissue histological analysis imply that neither the FGPNs nor the degradation products had acute toxicity. In brief, FGPNs perfectly integrated the capacities for PAI, SPECT, and MRI for diagnosis with

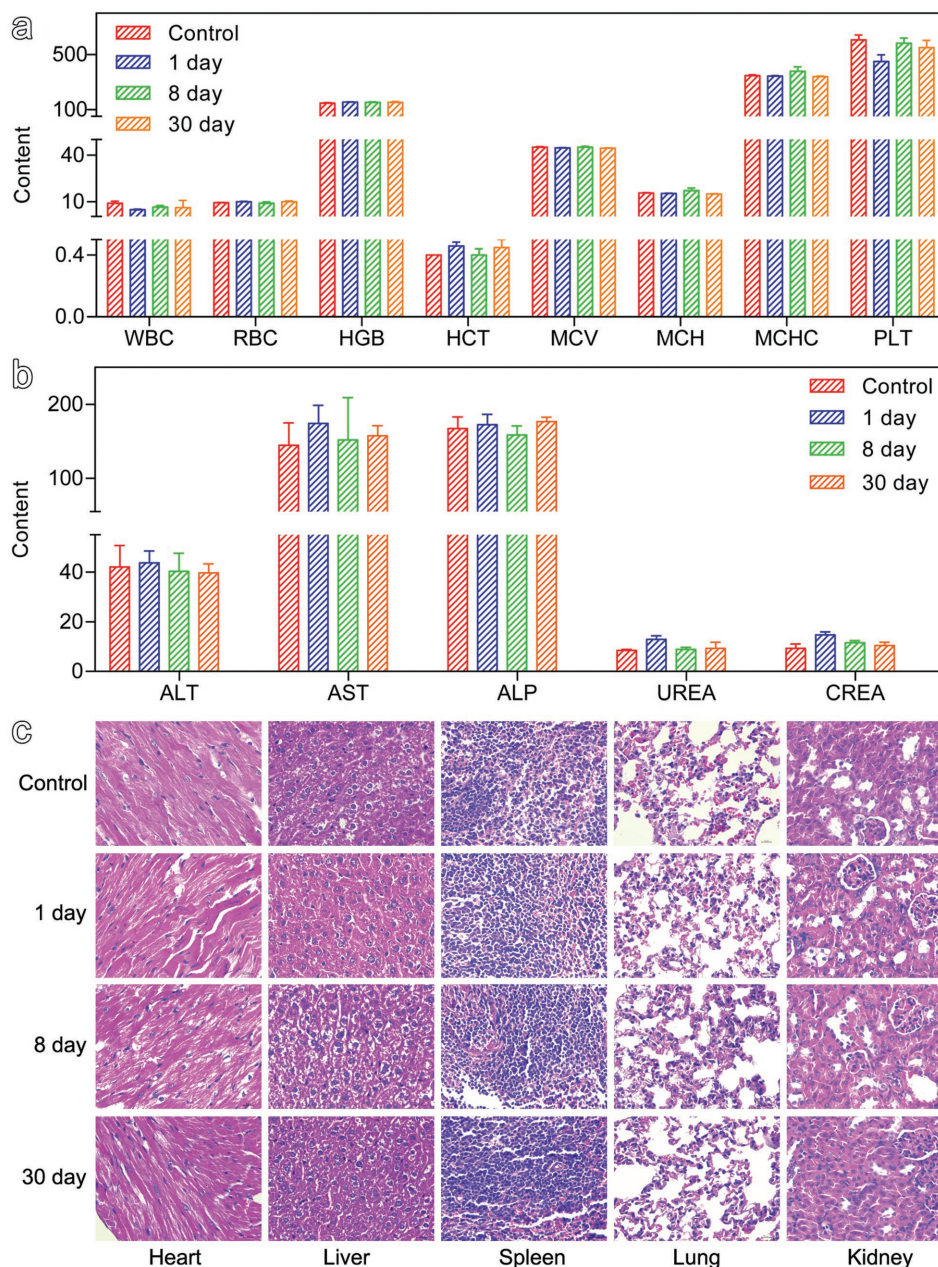


Figure 6. Biosafety assessment of FGPNs. a) Blood routine test results of mice treated with FGPNs. b) Blood biochemical test results of mice treated with FGPNs. c) H&E stained images of tissues from major organs of mice treated with FGPNs for comparing with those from mice receiving no treatment (control). Abbreviation: WBC, white blood cell; RBC, red blood cell; HGB, hemoglobin; HCT, hematocrit; MCV, mean corpuscular volume; MCH, mean corpuscular hemoglobin; MCHC, mean corpuscular hemoglobin concentration; PLT, platelets; ALT, alanine aminotransferase; AST, aspartate aminotransferase; ALP, alkaline phosphatase; UREA, urea; CREA, creatinine.

the outstanding photothermal conversion ability for tumor PTT, which highlights the potential in clinical translation for imaging-guided tumor therapy.

Supporting Information

Supporting Information is available from the Wiley Online Library or from the author.

Acknowledgements

L.C. and J.Y.C. contributed equally to this work. This work was supported by the National Natural Science Foundation of China (81530057, 21503141, 81430041, 81620108017, and 81471657), the National Key R&D Program of China (2016YFC0101200, 2016YFC0101201), Science and Technology Planning Project of Guangzhou (201604020098, 201610010006), and the China Postdoctoral Science Foundation (2015M570472, 2016T90489). All animal experiments reported herein were carried out according to the protocols approved by Soochow University Laboratory Animal Center.

Conflict of Interest

The authors declare no conflict of interest.

Keywords

coordination polymer nanoparticles, multimodality imaging, pharmacokinetics, radiolabeling, theranostic agents

Received: August 4, 2017

Revised: October 7, 2017

Published online: December 1, 2017

- [1] L. S. Wang, M. C. Chuang, J. A. A. Ho, *Int. J. Nanomed.* **2012**, 7, 4679.
- [2] E. Terreno, F. Uggeri, S. Aime, *J. Controlled Release* **2012**, 161, 328.
- [3] T. H. Kim, S. Lee, X. Y. Chen, *Expert Rev. Mol. Diagn.* **2013**, 13, 257.
- [4] L. Y. Rizzo, B. Theek, G. Storm, F. Kiessling, T. Lammers, *Curr. Opin. Biotechnol.* **2013**, 24, 1159.
- [5] N. Lee, D. Yoo, D. Ling, M. H. Cho, T. Hyeon, J. Cheon, *Chem. Rev.* **2015**, 115, 10637.
- [6] K. Yang, G. Yang, L. Chen, L. Cheng, L. Wang, C. Ge, Z. Liu, *Biomaterials* **2015**, 38, 1.
- [7] F. Y. Liu, X. X. He, H. D. Chen, J. P. Zhang, H. M. Zhang, Z. X. Wang, *Nat. Commun.* **2015**, 6, 8003.
- [8] D. Chen, C. Wang, X. Nie, S. Li, R. Li, M. Guan, Z. Liu, C. Chen, C. Wang, C. Shu, L. Wan, *Adv. Funct. Mater.* **2014**, 24, 6621.
- [9] P. Huang, J. Lin, W. Li, P. Rong, Z. Wang, S. Wang, X. Wang, X. Sun, M. Aronova, G. Niu, R. D. Leapman, Z. Nie, X. Chen, *Angew. Chem., Int. Ed.* **2013**, 52, 13958.
- [10] M. Zhou, R. Zhang, M. Huang, W. Lu, S. Song, M. P. Melancon, M. Tian, D. Liang, C. Li, *J. Am. Chem. Soc.* **2010**, 132, 15351.
- [11] L. Cheng, J. Liu, X. Gu, H. Gong, X. Shi, T. Liu, C. Wang, X. Wang, G. Liu, H. Xing, W. Bu, B. Sun, Z. Liu, *Adv. Mater.* **2014**, 26, 1886.
- [12] J. Liu, X. P. Zheng, L. Yan, L. J. Zhou, G. Tian, W. Y. Yin, L. M. Wang, Y. Liu, Z. B. Hu, Z. J. Gu, C. Y. Chen, Y. L. Zhao, *ACS Nano* **2015**, 9, 696.
- [13] M. Guo, H. Mao, Y. Li, A. Zhu, H. He, H. Yang, Y. Wang, X. Tian, C. Ge, Q. Peng, X. Wang, X. Yang, X. Chen, G. Liu, H. Chen, *Biomaterials* **2014**, 35, 4656.
- [14] J. Yu, C. Yang, J. Li, Y. Ding, L. Zhang, M. Z. Yousaf, J. Lin, R. Pang, L. Wei, L. Xu, F. Sheng, C. Li, G. Li, L. Zhao, Y. Hou, *Adv. Mater.* **2014**, 26, 4114.
- [15] K. Saatchi, P. Soema, N. Gelder, R. Misri, K. McPhee, J. H. E. Baker, S. A. Reinsberg, D. E. Brooks, U. O. Hafeli, *Bioconjugate Chem.* **2012**, 23, 372.
- [16] H. Gong, Z. Dong, Y. Liu, S. Yin, L. Cheng, W. Xi, J. Xiang, K. Liu, Y. Li, Z. Liu, *Adv. Funct. Mater.* **2014**, 24, 6492.
- [17] T.-H. Shin, Y. Choi, S. Kim, J. Cheon, *Chem. Soc. Rev.* **2015**, 44, 4501.
- [18] Y. Sheng, L. D. Liao, N. V. Thakor, M. C. Tan, *J. Biomed. Nanotechnol.* **2014**, 10, 2641.
- [19] Z. Gao, T. Ma, E. Zhao, D. Docter, W. Yang, R. H. Stauber, M. Gao, *Small* **2015**, 12, 556.
- [20] R. R. Qiao, C. H. Yang, M. Y. Gao, *J. Mater. Chem.* **2009**, 19, 6274.
- [21] Z. Gao, Y. Hou, J. Zeng, L. Chen, C. Liu, W. Yang, M. Gao, *Adv. Mater.* **2017**, 29, 1701095.
- [22] M. X. Yu, J. Zheng, *ACS Nano* **2015**, 9, 6655.
- [23] H. Arami, A. Khandhar, D. Liggitt, K. M. Krishnan, *Chem. Soc. Rev.* **2015**, 44, 8576.
- [24] M. L. Schipper, G. Iyer, A. L. Koh, Z. Cheng, Y. Ebenstein, A. Aharoni, S. Keren, L. A. Bentolila, J. Q. Li, J. H. Rao, X. Y. Chen, U. Banin, A. M. Wu, R. Sinclair, S. Weiss, S. S. Gambhir, *Small* **2009**, 5, 126.
- [25] T. Maldiney, C. Richard, J. Seguin, N. Wattier, M. Bessodes, D. Scherman, *ACS Nano* **2011**, 5, 854.
- [26] W. C. Xiao, J. Lin, M. L. Li, Y. J. Ma, Y. X. Chen, C. F. Zhang, D. Li, H. C. Gu, *Contrast Media Mol. Imaging* **2012**, 7, 320.
- [27] M. J. Ernsting, M. Murakami, A. Roy, S. D. Li, *J. Controlled Release* **2013**, 172, 782.
- [28] H. Soo Choi, W. Liu, P. Misra, E. Tanaka, J. P. Zimmer, B. Itty Ipe, M. G. Bawendi, J. V. Frangioni, *Nat. Biotechnol.* **2007**, 25, 1165.
- [29] E. Phillips, O. Penate-Medina, P. B. Zanzonico, R. D. Carvajal, P. Mohan, Y. Ye, J. Humm, M. Gönen, H. Kalaigian, H. Schöder, H. W. Strauss, S. M. Larson, U. Wiesner, M. S. Bradbury, *Sci. Transl. Med.* **2014**, 6, 260ra149.
- [30] C. Liu, Z. Gao, J. Zeng, Y. Hou, F. Fang, Y. Li, R. Qiao, L. Shen, H. Lei, W. Yang, M. Gao, *ACS Nano* **2013**, 7, 7227.
- [31] F. Mao, L. Wen, C. Sun, S. Zhang, G. Wang, J. Zeng, Y. Wang, J. Ma, M. Gao, Z. Li, *ACS Nano* **2016**, 10, 11145.
- [32] L. Wen, L. Chen, S. Zheng, J. Zeng, G. Duan, Y. Wang, G. Wang, Z. Chai, Z. Li, M. Gao, *Adv. Mater.* **2016**, 28, 5072.
- [33] X. Jiang, S. Zhang, F. Ren, L. Chen, J. Zeng, M. Zhu, Z. Cheng, M. Gao, Z. Li, *ACS Nano* **2017**, 11, 5633.
- [34] C. Zhou, G. Hao, P. Thomas, J. Liu, M. Yu, S. Sun, O. K. Öz, X. Sun, J. Zheng, *Angew. Chem., Int. Ed.* **2012**, 51, 10118.
- [35] E. B. Ehlerding, F. Chen, W. Cai, *Adv. Sci.* **2016**, 3, 1500223.
- [36] K. Briley-Saebo, A. Bjørnerud, D. Grant, H. Ahlstrom, T. Berg, G. Kindberg, *Cell Tissue Res.* **2004**, 316, 315.
- [37] D. Shen, J. Yang, X. Li, L. Zhou, R. Zhang, W. Li, L. Chen, R. Wang, F. Zhang, D. Zhao, *Nano Lett.* **2014**, 14, 923.
- [38] J. Llop, P. Jiang, M. Marradi, V. Gomez-Vallejo, M. Echeverria, S. Yu, M. Puigivila, Z. Baz, B. Szczupak, C. Perez-Campana, Z. Mao, C. Gao, S. E. Moya, *J. Mater. Chem. B* **2015**, 3, 6293.
- [39] J. Zeng, M. Cheng, Y. Wang, L. Wen, L. Chen, Z. Li, Y. Wu, M. Gao, Z. Chai, *Adv. Healthcare Mater.* **2016**, 5, 772.
- [40] X. Y. Lu, M. Niu, R. R. Qiao, M. Y. Gao, *J. Phys. Chem. B* **2008**, 112, 14390.
- [41] G. Ku, M. Zhou, S. L. Song, Q. Huang, J. Hazle, C. Li, *ACS Nano* **2012**, 6, 7489.
- [42] Y. M. Zhang, M. Jeon, L. J. Rich, H. Hong, J. M. Geng, Y. Zhang, S. X. Shi, T. E. Barnhart, P. Alexandridis, J. D. Huizinga, M. Seshadri, W. B. Cai, C. Kim, J. F. Lovell, *Nat. Nanotechnol.* **2014**, 9, 631.
- [43] Y. Zhou, D. P. Wang, Y. M. Zhang, U. Chitgupi, J. M. Geng, Y. H. Wang, Y. Z. Zhang, T. R. Cook, J. Xia, J. F. Lovell, *Theranostics* **2016**, 6, 688.
- [44] P. Caravan, J. J. Ellison, T. J. McMurphy, R. B. Lauffer, *Chem. Rev.* **1999**, 99, 2293.
- [45] Y. Hou, R. R. Qiao, F. Fang, X. X. Wang, C. Y. Dong, K. Liu, C. Y. Liu, Z. F. Liu, H. Lei, F. Wang, M. Y. Gao, *ACS Nano* **2013**, 7, 330.
- [46] R. B. Lauffer, *Chem. Rev.* **1987**, 87, 901.
- [47] M. Caicedo, J. J. Jacobs, A. Reddy, N. J. Hallab, *J. Biomed. Mater. Res., Part A* **2008**, 86A, 905.
- [48] K. Rajalakshmi, H. Devaraj, S. Niranjali Devaraj, *Food Chem. Toxicol.* **2001**, 39, 919.
- [49] B. Nair, *Int. J. Toxicol.* **1998**, 17, 95.
- [50] Y. Yang, Y. Sun, Y. Liu, J. J. Peng, Y. Q. Wu, Y. J. Zhang, W. Feng, F. Y. Li, *Biomaterials* **2013**, 34, 508.
- [51] T. Y. Cao, Y. Yang, Y. Sun, Y. Q. Wu, Y. Gao, W. Feng, F. Y. Li, *Biomaterials* **2013**, 34, 7127.
- [52] G. D. Zhang, Z. Yang, W. Lu, R. Zhang, Q. Huang, M. Tian, L. Li, D. Liang, C. Li, *Biomaterials* **2009**, 30, 1928.
- [53] J. F. Zeng, B. Jia, R. R. Qiao, C. Wang, L. H. Jing, F. Wang, M. Y. Gao, *Chem. Commun.* **2014**, 50, 2170.
- [54] C. Y. Liu, Z. Y. Gao, J. F. Zeng, Y. Hou, F. Fang, Y. L. Li, R. R. Qiao, L. Shen, H. Lei, W. S. Yang, M. Y. Gao, *ACS Nano* **2013**, 7, 7227.
- [55] N. Khlebtsov, L. Dykman, *Chem. Soc. Rev.* **2011**, 40, 1647.
- [56] P. A. Shore, B. B. Brodie, C. A. M. Hogben, *J. Pharmacol. Exp. Ther.* **1957**, 119, 361.